Experimental study and modeling of extreme ultraviolet 4000 lines/mm diffraction gratings coated with periodic and aperiodic Al/Mo/SiC multilayers

Amr Hisham K. Mahmoud, Sébastien de Rossi, Evgueni Meltchakov, Blandine Capitanio, Muriel Thomasset, Maxime Vallet, Franck Delmotte

▶ **To cite this version:**

HAL Id: hal-04355822
https://hal-iogs.archives-ouvertes.fr/hal-04355822

Submitted on 20 Dec 2023

Experimental study and modeling of extreme ultraviolet 4000 lines/mm diffraction gratings coated with periodic and aperiodic Al/Mo/SiC multilayers

AMR HISHAM K. MAHMOUD,[1] SÉBASTIEN DE ROSSI,[1] EVGUENI MELTCHAKOV,[1] BLANDINE CAPITANIO,[1,2] MURIEL THOMASSET,[2] MAXIME VALLET,[3,4] AND FRANCK DELMOTTE[1,*]

[1] *Université Paris-Saclay, Institut d'Optique Graduate School, CNRS, Laboratoire Charles Fabry, 91127, Palaiseau, France*

[2] *Synchrotron SOLEIL, L'Orme des Merisiers, Saint Aubin, BP 48F-91192 Gif sur Yvette Cedex, France*

[3] *Université Paris-Saclay, CentraleSupélec, CNRS, Laboratoire SPMS, 91190, Gif-sur-Yvette, France*

[4] *Université Paris-Saclay, CentraleSupélec, ENS Paris-Saclay, CNRS, LMPS - Laboratoire de Mécanique Paris-Saclay, 91190, Gif-sur-Yvette, France.*

*franck.delmotte@institutoptique.fr

Abstract: Multilayer coated diffraction gratings are crucial components for extreme ultraviolet (EUV) applications as spectroscopy or spectro-imaging. However, for high groove density, the smoothening of the grating surface profile with multilayer deposition remains a limitation that requires more investigation. In this paper, we report on the design, characterization, and modeling of 4000 lines/mm diffraction gratings coated with periodic and aperiodic Al/Mo/SiC multilayers for EUV radiation. Two types of gratings, with different groove depths are compared. Multilayer coatings were designed using a genetic algorithm to maximize the 1st -order diffraction efficiency in the 17-21 nm and in the 19-23 nm wavelength ranges at normal incidence. Periodic and aperiodic multilayers with different numbers of layers were deposited by magnetron sputtering on the 2 types of fused silica gratings and the grating groove profile evolution was measured by atomic force microscopy, and by cross-section transmission electron microscopy. The first-order diffraction efficiency was measured in the EUV at 5° incidence using monochromatic synchrotron radiation and modeled using the Rigorous Coupled-Wave Analysis method. The simulation models refined by using the Debye-Waller factor to account for the multilayer interfacial roughness show a good agreement with experimental data. The results reported in this study will allow for designing efficient EUV multilayer gratings for high-resolution spectro-imaging instruments.

1. Introduction

The development of multilayer-coated gratings for X-rays and extreme ultraviolet (EUV) radiation is crucial for several applications that require high spectral resolution: spectroscopy, beamsplitters or monochromators for synchrotron radiation sources, spectro-imagers for space science, etc. [1–3]. Indeed, soft x-ray and EUV multilayer gratings that satisfy both the grating diffraction and multilayer Bragg interference requirements provide higher diffraction efficiency when compared to single-layer coated gratings [4–6]. Several types of multilayer grating have been theoretically and experimentally studied such as blazed multilayer gratings [7,8], sliced multilayer gratings [9], lamellar or trapezoidal multilayer gratings [5, 10], and alternate multilayer gratings for tender x-rays [11–13].

In the past, several material combinations have been reported to achieve high reflectance in the EUV for multilayer-coated mirrors. Among them, Al/Mo/SiC multilayers provide high reflectance and good stability in the wavelength range 17 nm – 40 nm, a region of particular interest for solar physics [14,15]. Recently, we have demonstrated that 3600 l/mm gratings coated

with Al/Mo/SiC multilayer provide high diffraction efficiency around 27 nm wavelength [6].This study was limited to one type of grating with a groove depth of around 20 nm. We have shown that the peak efficiency was limited by the smoothening of the initial trapezoidal surface profile as a function of the number of multilayer periods. We have also reported that a grating coated with a 12-layer aperiodic multilayer provides broader efficiency as compared to a periodic multilayer. Though, the following important questions were not addressed in our initial study: how do the groove density and the groove depth impact the evolution of the surface profile and the experimental diffraction efficiency? How does the interfacial roughness affect the diffraction efficiency of the grating? Can aperiodic coatings with more layers increase the broadband efficiency of the grating?.

In this paper, we report on the characterization and modeling of multilayer gratings with high efficiency between 17 nm and 23 nm wavelength at near-normal incidence and we attempt to respond to the previous questions. We compare the properties of periodic and aperiodic Al/Mo/SiC multilayer designs deposited on fused silica grating samples with higher groove density and with 2 different groove depth configurations.

In this paper, we report on the characterization and modeling of multilayer gratings with high efficiency between 17 nm and 23 nm wavelength at near normal incidence. We compare the properties of periodic and aperiodic Al/Mo/SiC multilayer designs deposited on fused silica grating samples.
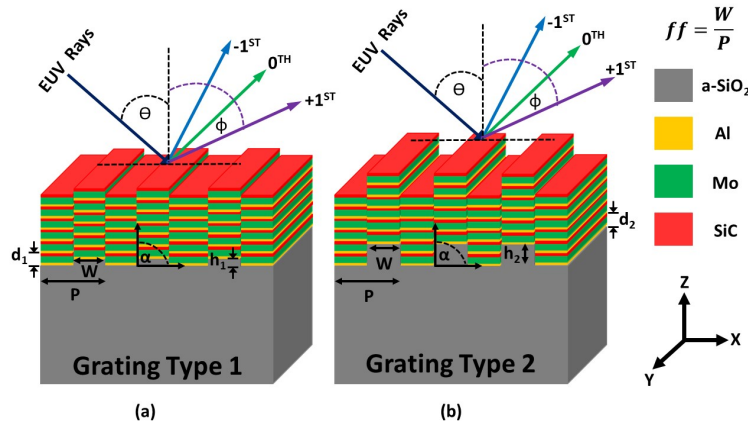

Fig. 1. schematic diagram for the gratings with periodic multilayers ($N = 6$) at two different grating heights (a) type 1 and (b) type 2.

The diagram in Fig.1 illustrates the structure of periodic Al/Mo/SiC multilayers deposited on amorphous silica grating of two different groove depths (type 1 and type 2). The incident photons are directed perpendicularly to the grooves of the grating with an angle of incidence θ, and diffracted into +1, 0, and -1 orders at an angle ϕ. Both types of gratings have the same width (W), periodicity (P), and full-width half maximum fill factor ($ff = W/P$). α represents the grating slope. $\alpha = 90°$ correspond to a lamellar grating while $\alpha < 90°$ correspond to a trapezoidal grating. Each type of grating has a different grating depth (h) and a different multilayers period (d). Grating type 1 corresponds to a depth equal to half of the multilayer period ($h_1 = 0.5d_1$), while grating type 2 corresponds to a depth equal to three halves of the multilayer period ($h_2 = 1.5d_2$). Theoretically, for an ideal structure, both types of grating should provide similar diffraction efficiency. However, in practice, the slopes of the trapezoidal profile, the number of deposited layers, and the type of design (periodic vs aperiodic) may have a different impact on the diffraction efficiency for each type of grating. One objective of this study is to highlight the distinct advantages of each grating type for EUV applications, such as the Solar C

mission, targeting the 19 nm wavelength range [16].

After a brief description of the simulation and experimental tools, we present the design, characterization, and modeling of the multilayer coatings deposited on flat substrates. Then, we study the evolution of the grating profile after multilayer deposition by means of atomic force microscopy (AFM) and transmission electron microscopy (TEM). The +1-order diffraction efficiency of the periodic and aperiodic multilayer gratings has been measured at 5° incidence using EUV monochromatic synchrotron radiation measurements. Finally, we propose a model for the +1-order diffraction efficiencies using Rigorous coupled-wave analysis (RCWA) and Debye-Waller (DW) approximation and compare it with experimental results.

2. Simulation tools

The optimization of Al/Mo/SiC over a silica flat substrate is accomplished by the IMD software [17] for periodic and aperiodic designs. The optimization process was carried out using a genetic algorithm, without taking into account interfacial roughness, with the aim of achieving maximum reflectance over a specific wavelength domain at normal incidence. For grating type 1, the wavelength range was between 17 nm and 21 nm, while for grating type 2, it was between 19 nm and 23 nm. We used optical constants from references [17, 18], with densities of 2.7 g/cm^3 for Al, 10.22 g/cm^3 for Mo, and 3.22 g/cm^3 for SiC.

To simulate multilayer over trapezoidal grating, a homemade MATLAB code is combined with an open-source RCWA software [19] without considering interfacial roughness. This code has been discussed in a previous paper [6].

3. Experimental setup

Two sets of 4000 lines/mm grating substrates were manufactured by ZEISS, each one with a different groove depth. The fabrication process included initial spin coating, followed by holographic exposure, ion beam etching, and cleaning in O_2 plasma. We used three samples, with dimensions of 20x20x6 mm^3, in each set. The specification for the groove depths, respectively 4.4 nm ±10% and 14.4 nm ±10% correspond to the two types of gratings shown in Fig.1 for a central wavelength of 19 nm. The grooves of both grating types have a trapezoidal shape, and the initial surface roughness of the substrate is less than or equal to 0.2 nm.

Both periodic and aperiodic multilayers were deposited on flat silicon (Si) or fused silica (SiO$_2$) grating substrates using a Plassys® MP800 magnetron sputtering machine in an ISO6 cleanroom facility at Laboratoire Charles Fabry. The flat Si substrates used were Si wafer pieces measuring 20x20 mm^2, with a thickness of 1 mm and a (100) crystal orientation. The surface microroughness of the substrates was in the range of 0.3 nm. The grating samples were coated with two different multilayer coatings on each half using a mask during the deposition process. The deposition parameters and sputtering machine geometry have been previously described [14, 20]. The deposition process employed SiC and Mo targets with a purity of 99.5% and 99.95%, respectively, and a Si-doped (1.5 wt. %) Al target with a purity of 99.99%. The plasma discharge was established using an argon pressure of 2 mTorr, a DC-Current of 0.06 A, and RF power of 200 W and 150 W for the Mo, Al, and SiC targets, respectively.

GIXR was carried out using a Discover D8 diffractometer from BRUKER®. The diffractometer was fitted with a Cu Kα radiation source having a wavelength of 0.154 nm, a rotary absorber, Soller and divergence slits, a collimating Gobel mirror, and a scintillator. The reflectance curves were analyzed in the specular configuration, with grazing angles ranging from 0 to 6 degrees, in steps of 0.01 degrees. The GIXR data was analyzed using the IMD software [17].

The grating samples were characterized using atomic force microscopy (AFM) in non-contact mode, utilizing the AFM NX 20 from Park System company. The measurements were performed in an ISO7 cleanroom at SOLEIL Synchrotron, and the image sizes were 2x2 μm^2. The AFM data were analyzed using WSxM 5.0 software [21] to determine various grating parameters such

127 as top and bottom roughness, groove depth (d), fill factor (ff), and the slope of the trapezoidal
128 (α). The surface morphology underwent multiple processes by WSxM 5.0 software to achieve
129 the grating profile. These processes included rotating the image to align the grooves vertically
130 and subsequently averaging the groove profiles in a selected area.

131 Two grating samples with Al/Mo/SiC periodic multilayer were measured by transmission
132 electron microscopy (TEM). The cross-section samples were prepared using an FEI ThermoFisher
133 Helios Nanolab 660 and a Pt layer was deposited on top of the multilayer to protect it during
134 the ion beam etching process. Energy dispersive x-ray spectrometry (EDX) was carried out in
135 scanning TEM (STEM) mode using an FEI ThermoFisher Titan3 G2 80-300 microscopy with Cs
136 probe corrector and Super X EDX detector operating at 300 kV.

137 The multilayer-coated Si samples and gratings were also characterized by soft x-ray reflec-
138 tometry (SXR) at the Metrology and Tests beamline, SOLEIL synchrotron. The experimental
139 conditions used were the same as in Ref. [6]. The suppression of high harmonics was achieved
140 using a 0.5 μm Al filter and a 3-mirror low-pass filter that utilized the Si-coated strips. The
141 input and output mirrors of the low pass filter were set at an angle of incidence of 3.5°. A
142 detector consisting of an Al-coated Si photodiode was used, and the calibration in the energy of
143 the monochromator was confirmed by measuring the position of the Al $L_{2,3}$ absorption edge.
144 The beam was estimated to be 96% s-polarized [6]. To measure the diffraction efficiencies, the
145 detector was rotated with a fixed incidence angle and wavelength to scan the order of diffraction
146 of interest. These detector scans were repeated for each wavelength in the range of interest.

4. Multilayer Design

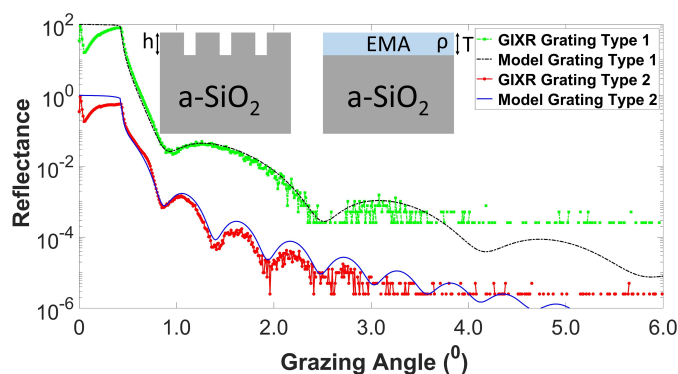### 4.1. Initial parameters for the design

Fig. 2. GIXR measurements and the EMA model were conducted for both grating types
without multilayers. The data for grating type 1 and its corresponding model have been
shifted by 10^2 units.

149 Initially, one sample of each grating type has been characterized before the deposition with
150 GIXR as shown in Fig.2. The effective medium approximation model (EMA) [22] has been used
151 to extract some information such as thickness (T) and density (ρ) of the effective layer which
152 represents the grating height and fill factor, respectively. The results are shown in Table 1 indicate
153 that grating type 1 and grating type 2 have averaged heights of 5.3 nm and 16.1 nm respectively.
154 It should be noted that SiO$_2$ has a theoretical density of 2.2 g/cm^3 [18]. Thus, if the grating were
155 perfectly symmetrical ($f.f = 0.5$), the density of the effective layer would be 1.1g/cm^3. The fact
156 that the densities of the effective layer are less than 1.1 g/cm^3 indicates that the fill factor is less
157 than 0.5 for both types of gratings. It is noteworthy that the T values obtained through the EMA

Table 1. The effective layer thickness (T), density (ρ), and roughness (σ_{layer}) along with the substrate roughness ($\sigma_{\text{substrate}}$) were obtained using the EMA model.

Grating Type	T (nm)	ρ (g/cm^3)	$\sigma_{\text{substrate}}$ (nm)	σ_{layer} (nm)
1	5.3	0.90	0.3	0.45
2	16.1	0.75	0.2	0.5

model are in good agreement with the groove depth measured by AFM before deposition and are higher than the specified values for both types of gratings.

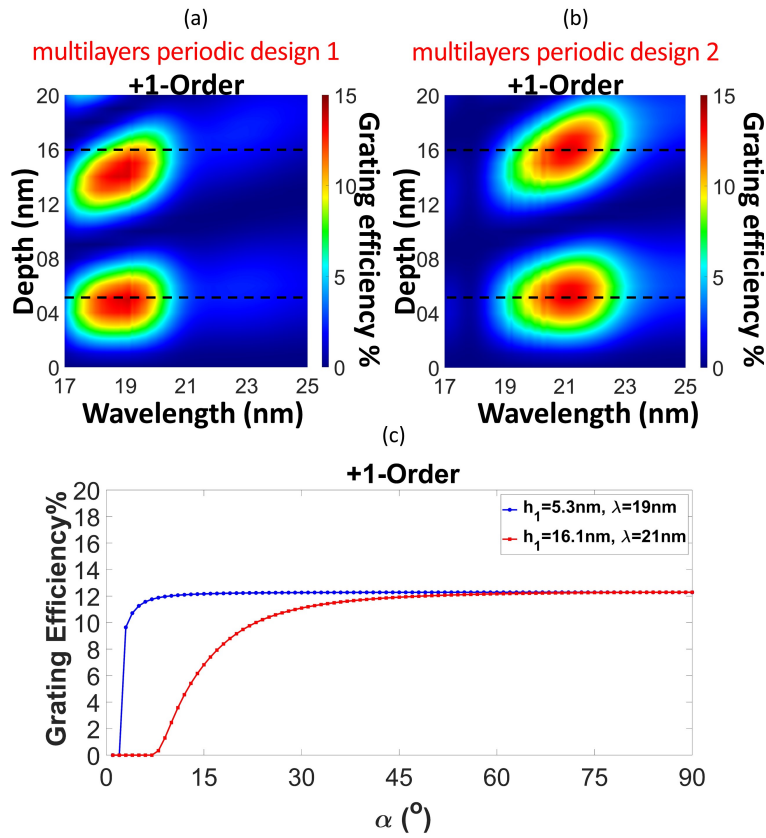## 4.2. Periodic multilayer design

Fig. 3. RCWA simulations were employed to analyze the correlation between wavelength, grating efficiency, and grating depth for multilayers on lamellar gratings with $N = 6$ periods, specifically considering (a) multilayers periodic design 1 and (b) multilayers periodic design 2, while at (c) The grating efficiency influenced by grating slope (α) for multilayer gratings with $N = 6$ periods, with a focus on multilayers periodic design 1 at ($h_1 = 5.3nm$, $\lambda = 19nm$) and multilayers periodic design 2 at ($h_2 = 16.1nm$, $\lambda = 21nm$).

For this study, a periodic Al/Mo/SiC multilayer was optimized by IMD to achieve the best broadband reflectance in the wavelength range of 17-21 nm. The initial number of periods for the optimization was fixed to 6 ($N = 6$), as it was found to be the optimal number of periods in a previous experimental study [6]. The optimized thicknesses were found to be 3.84 nm, 4.33 nm, and 1.99 nm for Al, Mo, and SiC, respectively. A 1 nm SiC is added to the top SiC layer to create a final 3 nm thick top SiC layer, offering protection against oxidation and diffusion. This protective layer is needed for ensuring the long-term stability of the multilayers [23]. The +1-order diffraction efficiency of this optimized multilayer structure deposited on a grating substrate was simulated by RCWA with parameters of $N = 6$, $P = 250$ nm, and $ff = 0.5$. The results plotted in Fig.3(a) showed good broadband efficiency for grating type 1 ($h_1 = 5.3$ nm), but poor results for grating type 2 ($h_2 = 16.1$ nm), especially in wavelengths ranging from 17 nm to 19 nm. Note that the diffraction efficiency pattern is more symmetrical for type 1 than for type 2. This indicates that for applications that require broadband diffraction efficiency, grating type 1 will be less sensitive to errors in groove depth. Therefore, the thickness of the multilayers was re-optimized for grating type 2 by shifting the wavelength by 2 nm to target the highest broadband reflectance in the wavelengths 19-23 nm. These new multilayer thicknesses were found to be 5.01 nm, 4.37 nm, and 1.99 nm for Al, Mo, and SiC, respectively, with a 1 nm protection layer of SiC. The +1-order diffraction efficiency is plotted in Fig.3(b) as a function of groove depth and wavelength and shows high broadband efficiency for grating type 2 in wavelengths ranging from 19 nm to 23 nm. The variation of +1-order diffraction efficiency with α is also plotted in Fig.3(c) for each grating. Grating type 1 ($h_1 = 5.3$ nm) provides high efficiency even with small values of angles α. In contrast, grating type 2 ($h_2 = 16.1$ nm) shows low efficiency for angles α lower than 15 degrees.

4.3. Aperiodic multilayer design

Recent literature has shown that the theoretical study of aperiodic multilayers on the grating demonstrates interesting wideband efficiency [6, 24, 25]. The IMD software was used to optimize two aperiodic designs for each type of grating. The thickness of each layer in the optimized multilayer designs is shown on the y-axis, and the position in the multilayer stack is indicated in the x-axis in Fig.4. The thickness of Al, Mo, and SiC layers are plotted respectively in blue, red, and green. For each design, the top SiC layer is about 3 nm thick, ensuring the long-term stability of the multilayers [23].

In Fig.4(a) and Fig.4(b), the optimized multilayer designs for grating type 1 are shown. Fig.4(a) shows the thickness of each layer for a 18-layer design, while Fig.4(b) shows the thickness of each layer for a 24-layer design. The optimized designs aim to achieve broadband efficiency from 17-21 nm.

Similarly, in Fig.4(c) and Fig.4(d), the optimized multilayer designs for grating type 2 are shown. Fig.4(c) shows the thickness of each layer for an 18-layer design, while Fig.4(d) shows the thickness of each layer for a 24-layer design. The optimized designs aim to achieve broadband efficiency from 19-23 nm.

4.4. Comparison of periodic and aperiodic multilayer reflectance

The simulation results for various periodic and aperiodic multilayers with N values of 4, 6, 8, and 10 on a flat Si substrate, without considering the material roughness, are shown in Figs.5(a-b). Fig.5(a) shows the broadband reflectance ranging from 17-21 nm, which is applicable for grating type 1, while Fig.5(b) demonstrates the wideband reflectance from 19-23 nm, appropriate for deposition on grating type 2.
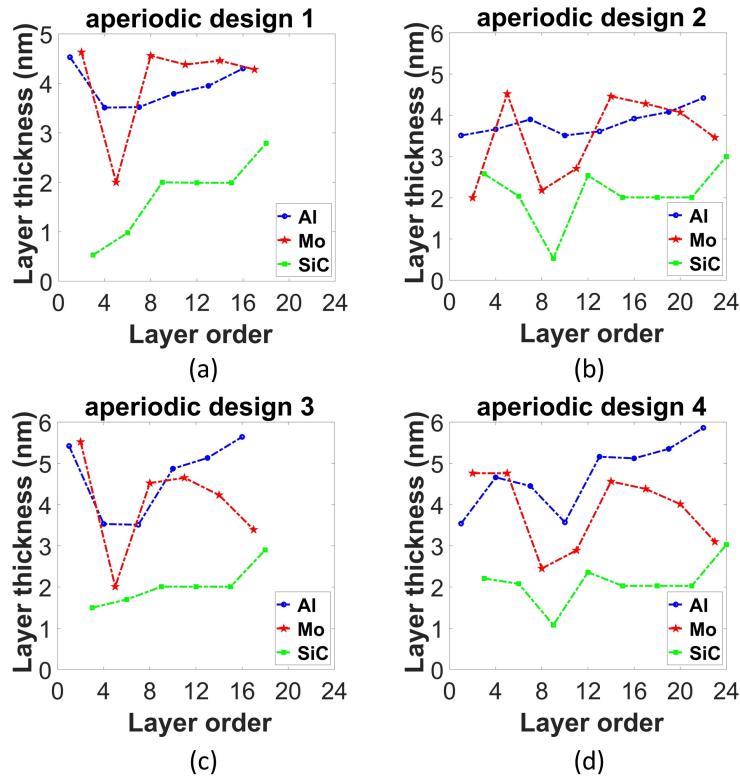
Fig. 4. depth distribution of layer thicknesses in the aperiodic multilayer structures for (a) design 1, (b) design 2, (c) design 3, and (d) design 4.
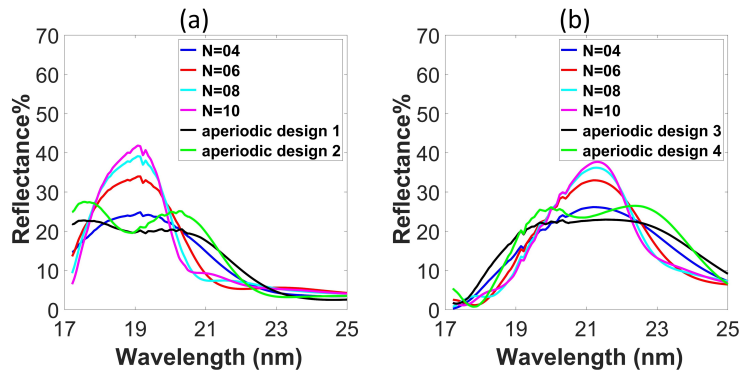

Fig. 5. Simulated reflectance of optimized periodic Al/Mo/SiC multilayers with varying numbers of periods and aperiodic Al/Mo/SiC multilayers is presented as a function of wavelength at $\theta = 5°$, intended for use with (a) grating type 1 and (b) grating type 2.

5. Multilayer deposition and modeling

In order to assess the quality of the multilayer structures used for grating type 1, three different samples have been deposited on flat silicon substrates: periodic (samples MP21074, $N = 10$), 18-layer aperiodic (sample MP21076), and 24-layer aperiodic (sample MP21082). GIXR and SXR were used to characterize the three test samples, and the results are shown in Fig.6(a) and

Table 2. Layer thickness and interfacial roughness values used to model the periodic test samples for grating type 1 and 2.

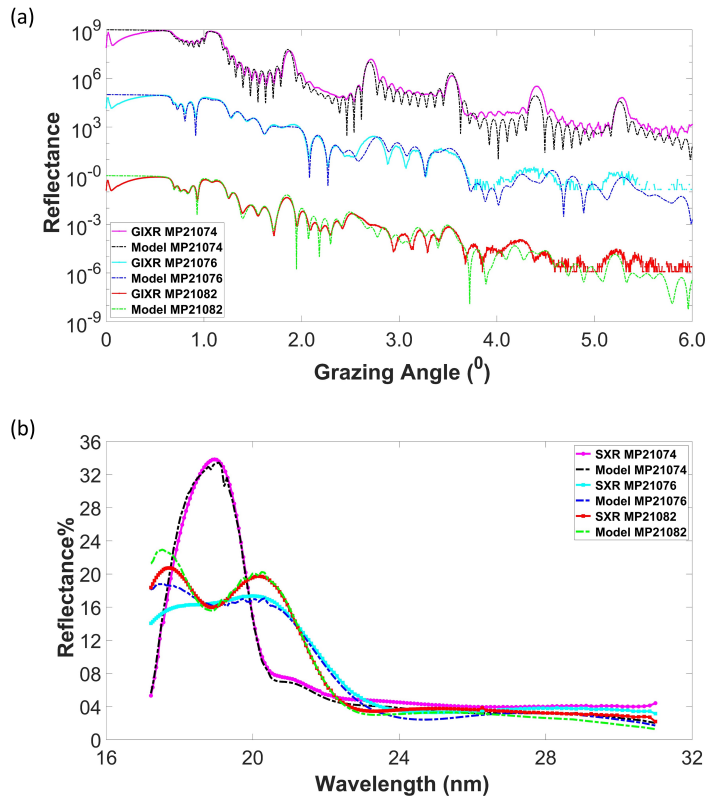| Material	Design 1 Thickness	Design 2 Thickness	Interface	Roughness
Top Oxide layer	0.50 nm	0.50 nm	Top surface	0.30 nm
SiC	1.99 nm	1.99 nm	Oxide-on-SiC	0.30 nm
			& Al-on-SiC	
Mo	4.33 nm	4.37 nm	SiC-on-Mo	0.60 nm
Al	3.84 nm	5.01 nm	Mo-on-Al	0.70 nm
Si Substrate	∞	∞	Al-on-Si substrate	0.35 nm

Fig. 6. illustrates the measured and fitted curves for three different multilayer samples: the 10-period Al/Mo/SiC multilayer (sample MP21074), the 18-layer aperiodic Al/Mo/SiC multilayer (sample MP21076), and the 24-layer aperiodic Al/Mo/SiC multilayer (sample MP21082). Subfigure (a) presents the GIXR curves at $\lambda = 0.154$ nm, with samples MP21076 and MP21074 being shifted by 10^5 and 10^9, respectively. Subfigure (b) displays the SXR curves at $\theta = 5°$.

Fig.6(b) respectively. The IMD models for the three samples are also plotted in Fig.6 and are in good agreement with the measured data. The models use theoretical material thicknesses for the periodic and aperiodic designs (see Table.2 and Fig.4). The thickness of the top oxide layer used to model MP21074, MP21076, and MP21082 was 0.5 nm, 0.6 nm, and 0.9 nm, respectively. The model used for the periodic multilayer (MP21074) includes a cap layer of SiC with a thickness of 0.99 nm on the top of the last SiC layer. The discrepancy observed around 17 nm between the modeled and measured data for aperiodic multilayer designs may be due to the inaccuracy in Al optical constants near the $L_{2,3}$ absorption edge (as indicated in reference [26]), or to the potential difference between the targeted and actual thickness of layers in the aperiodic design.
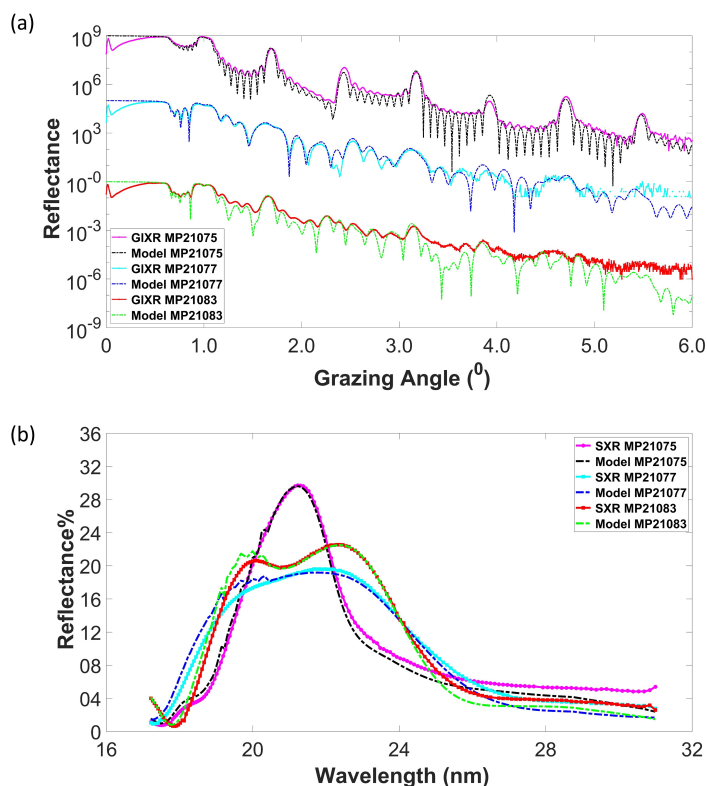

Fig. 7. displays the measured and fitted curves for three distinct multilayer samples: the 10-period Al/Mo/SiC multilayer (sample MP21075), the 18-layer aperiodic Al/Mo/SiC multilayer (sample MP21077), and the 24-layer aperiodic Al/Mo/SiC multilayer (sample MP21083). In subfigure (a), GIXR curves at $\lambda = 0.154$ nm are presented, with samples MP21077 and MP21075 being shifted by 10^5 and 10^9, respectively. Subfigure (b) shows SXR curves at $\theta = 5°$.

In a similar manner, periodic (sample MP21075, $N = 10$), 18-layer aperiodic (sample MP21077), and 24-layer aperiodic (sample MP21083) structures were deposited on silicon substrates to investigate the quality of multilayers for grating type 2. GIXR and SXR measurements are shown in Fig.7 with the IMD models. The models use theoretical material thicknesses for the periodic and aperiodic designs. The thicknesses of the oxide layer used to model MP21075, MP21077, and MP21083 were 0.5 nm, 0.8 nm, and 0.7 nm, respectively. The same interfacial roughness values were used to model the 6 samples (MP21074, MP21076, MP21082, MP21075, MP21077, and MP21083). In the periodic multilayer model (MP21075), a SiC cap layer is

228 featured, with its thickness calculated by the model as 0.99 nm, positioned above the top SiC
229 layer. These interfacial roughness values are given in Table.2.

6. Al/Mo/SiC multilayer gratings

6.1. Evolution of the grating surface profile after periodic multilayer deposition
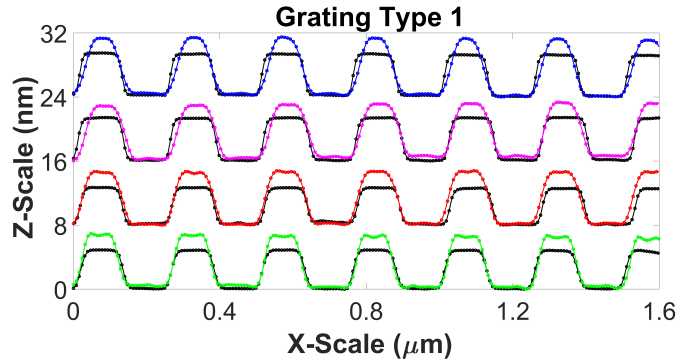

Fig. 8. AFM average groove profiles before (black) and after (colored) the deposition
of periodic Al/Mo/SiC multilayer for grating type 1 as a function of the number of
periods; every profile is shifted by 8 nm in Z-Scale.

232   The grating profiles of grating type 1 samples were measured before and after multilayer
233 deposition by AFM and are displayed in Fig.8. The groove profiles before deposition are shown
234 in black and the ones after deposition are shown in colored lines: green represents $N = 4$, red
235 represents $N = 6$, pink represents $N = 8$, and blue represents $N = 10$. The shape of the profile
236 after deposition appears to be trapezoidal for $N = 4, 6$, and 8. However, the profile starts to have
237 a sinusoidal shape on the top part for $N = 10$. The evolution of the grating profile shape (from
238 trapezoidal to sinusoidal) is consistent with previous results reported in the case of Al/Mo/SiC
239 multilayer on a 3600 l/mm grating with 21 nm groove depth [6]. Fig.8 also reveals that the depth
240 of the grooves at the surface of the multilayer grating is increased compared to the depth of the
241 grooves in the grating before deposition. This increase could be attributed to the fact that the
242 period thickness of the multilayer is almost twice the depth of the grooves in the original grating.
243 That difference may have an impact on the profile evolution of the multilayer grating.
244   In relation to aperiodic designs 1 and 2 as applied to grating type 1, a consistent trend was
245 observed: the depth increased after deposition compared to its initial state prior to deposition.
246 Additionally, the profile maintained its trapezoidal shape, corresponding to the profile shape of
247 the periodic designs with ($N = 6$) and ($N = 8$), both possessing the same number of layers.
248   In Fig.9 the grating profiles for grating type 2 before and after deposition are shown. The
249 groove profiles are shown before (in black) and after (in color): green for $N = 4$, red for $N = 6$,
250 pink for $N = 8$, and blue for $N = 10$. The results indicate that the profiles after deposition change
251 to the sinusoidal shape for all N except $N = 4$, which remains a trapezoidal profile. In the case of
252 $N = 6$ and $N = 8$, the depth of the grooves in the multilayer grating is also increased compared
253 to the depth of the grooves in the grating before deposition. However, for $N = 4$ and $N = 10$,
254 the change is not as pronounced. This difference in behavior could be attributed to the higher
255 roughness values of $N = 6$ and $N = 8$ samples, as shown in Table.6 in the appendix. It is worth
256 noting that $N = 6$ and $N = 8$ was deposited on different halves of the same grating sample. These
257 results suggest that the evolution of the grating profile (in shape and height) depends on the initial
258 grating roughness and on the individual layer thicknesses. In order to get more insight into these
259 phenomena, we performed TEM analyses on two grating samples, one of each type.
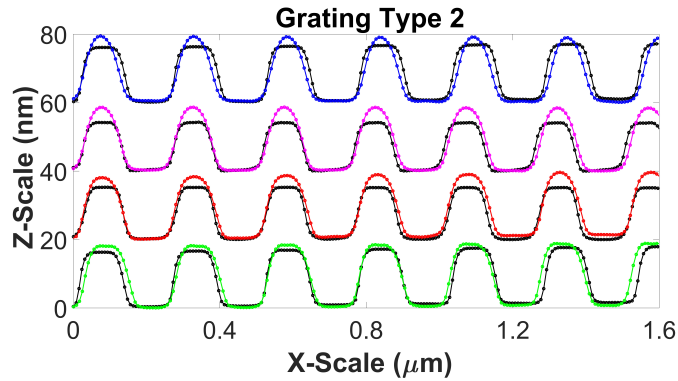
Fig. 9. AFM average groove profiles before (on black) and after (on colored) the deposition of Al/Mo/SiC for grating type 2 as a function of the number of periods; every profile is shifted by 20 nm in Z-Scale.

In relation to aperiodic designs 3 and 4 applied to grating type 2, a comparable pattern emerged where the depth exhibited an increase following deposition, in contrast to its initial depth before deposition. Additionally, the profile transitioned from a trapezoidal shape to a superior top sinusoidal configuration. The profile shape obtained for aperiodic designs 3 and 4 is consistent with the profile shape of the periodic designs with $N = 6$ and $N = 8$, both having an identical number of layers.
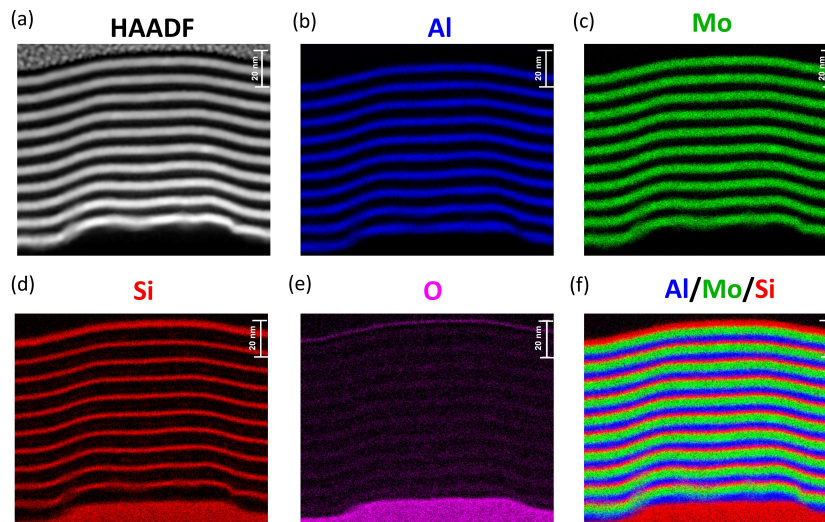

Fig. 10. STEM analyses on multilayer grating type 1 with 10 periods ($N = 10$) including (a) HAADF image and (b-f) energy-dispersive X-ray spectroscopy (EDX) images of individual elements: (b) aluminum (Al), (c) molybdenum (Mo), (d) silicon (Si), (e) oxygen (O), and (f) composite images of Al/Mo/Si. The scale bars represent 20 nm.

Fig.10 and Fig.11 depict the TEM images for the 10-period multilayer on grating type 1 and grating type 2, respectively. Fig.10(a) and Fig.11(a) display the high-angle annular dark-field (HAADF) scanning transmission electron microscopy (STEM) image of both samples. In HAADF, the high-density Mo layers appear bright, while the low-density Al and SiC layers
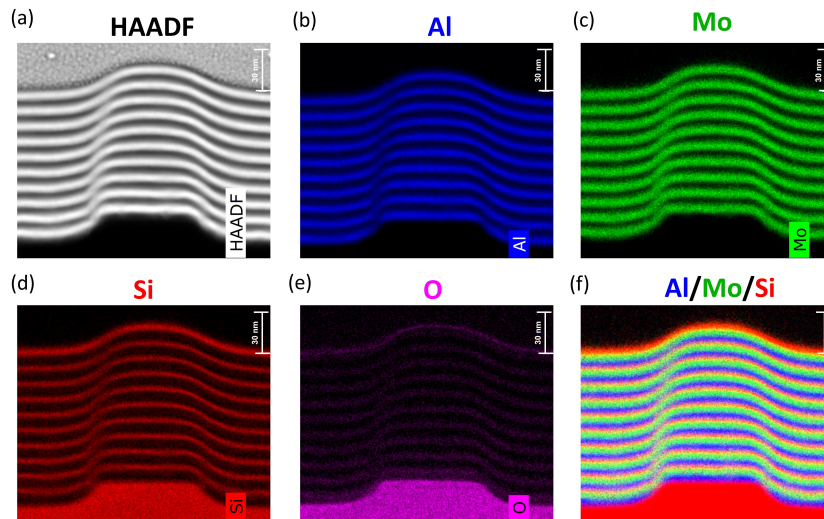
Fig. 11. STEM analyses for multilayer grating type 2 with 10 layers ($N = 10$) including: (a) HAADF image, and (b-f) EDX images of individual elements: (b) Al, (c) Mo, (d) Si, (e) O, and (f) composite images of Al/Mo/Si. The scale bars represent 30 nm.

appear dark.

Furthermore, the specific atom locations can be identified individually by EDX-STEM analysis. The EDX analysis identified the materials Al, Mo, Si, and O, which are plotted separately in Figs.10(b-f) and Figs.11(b-f). The EDX analysis results show the presence of an oxidation layer at the top of the multilayer on the grating (Fig.10(e) and Fig.11(e)) and the evolution of the deposition of the materials on the gratings' profile.

It is worth noting that the 3600 l/mm multilayer grating studied previously [6] did not exhibit any change of groove depth after deposition of up to 16 periods. Thus, the reduction of the grating period from 277.7 nm to 250 nm seems to have a significant impact on the growth process.

In Fig.10(a), it is clear that the trapezoidal profile displays noticeable asymmetry and tilt towards the left. The profile remains approximately trapezoidal from $N = 1$ to $N = 6$. However, when the number of periods increases above 7, the grating profile transitions to a sinusoidal shape at the top. In Fig.11(a), the asymmetry of the trapezoidal grating is clearly visible, the slopes on the left side being larger than the slopes on the right side. The profile keeps its trapezoidal shape from $N = 1$ to $N = 3$. However, after deposition of 4 or 5 periods, the grating's profile transitions to a more rounded shape at its edges. When N reaches 6, the grating profile changes to a sinusoidal shape at the top. These observations are consistent with the AFM measurements reported in Fig.9. It is also interesting to note that, for both types of gratings, the top profile of the multilayer grating shifts towards the right with increasing N. This phenomenon that has already been reported and may be due to a phenomenon has been reported previously [5, 8] and may be attributed to the fact that the average direction of atomic flux is not perfectly normal to the surface of the substrate.

In Figs.10(b-f), the individual layers are well defined and transitions between layers appear to be sharp except for the first period on the substrate. We can clearly see roughness on the top of the first Al layer that propagates to the next Mo and SiC layers as shown in Fig.10(b). However, the deposition of the following periods smoothed up the interfaces and, for $N = 2$ to $N = 10$, minimal roughness or interdiffusion is observed on the top, bottom, and slopes of the multilayer gratings.

The EDX-STEM images in Fig.11(b-f) demonstrate that the depositions of Al, Mo, and SiC

exhibit a uniform appearance, with no noticeable interdiffusion or roughness on the top, bottom, or right slope of the trapezoidal gratings. Nevertheless, interdiffusion becomes apparent on the left side of the slope where the three deposited materials appear to interdiffusion. Moreover, the first Al layer doesn't exhibit any significant roughness as compared with grating type 1. This may be attributed to the fact that the Al layer in grating type 2 is thicker than in grating type 1.
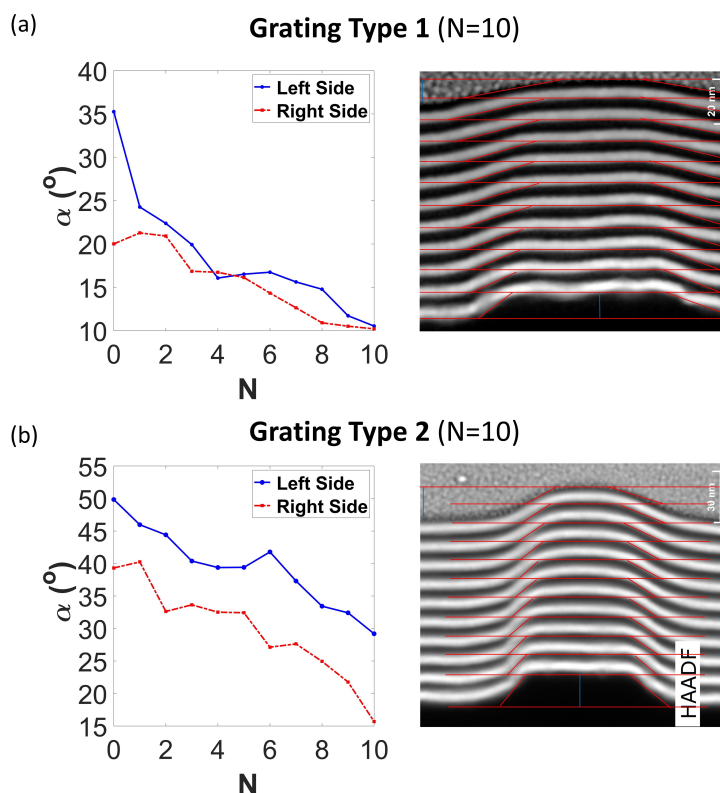

Fig. 12. The computed values of α from STEM analyses for the multilayer with $N = 10$ are shown for (a) grating type 1 with a 20 nm HAADF scale bar and (b) grating type 2 with a 30 nm HAADF scale bar.

The value of the trapezoidal slope α is an important parameter that affects the efficiency of diffraction gratings. We have computed α from the left and right sides of the trapezoidal for both types of gratings (grating type 1 and 2). The slope was estimated from the red lines on the HAADF image (shown as insets on Fig.12) using the Fiji software [27]. Fig.12(a) shows the α evolution from the grating surface ($N = 0$) to the last period of Al/Mo/SiC at $N = 10$ for grating type 1. It can be observed that α decreases almost linearly for both sides as N increases. The same observation has been made for grating type 2 in Fig.12(b). In this case, the asymmetry of the 2 slopes appears clearly. Note that the initial slopes of the grating substrates are significantly higher for grating type 2 than for grating type 1. This difference is also confirmed by AFM measurements.

6.2. Multilayer grating diffraction efficiency: results and modeling

The SXR measurements of the +1-order diffraction efficiency of the 6 samples of grating type 1 (respectively type 2) at normal incident angle $\theta = 5°$ are shown in Fig.13 (resp. Fig.14).

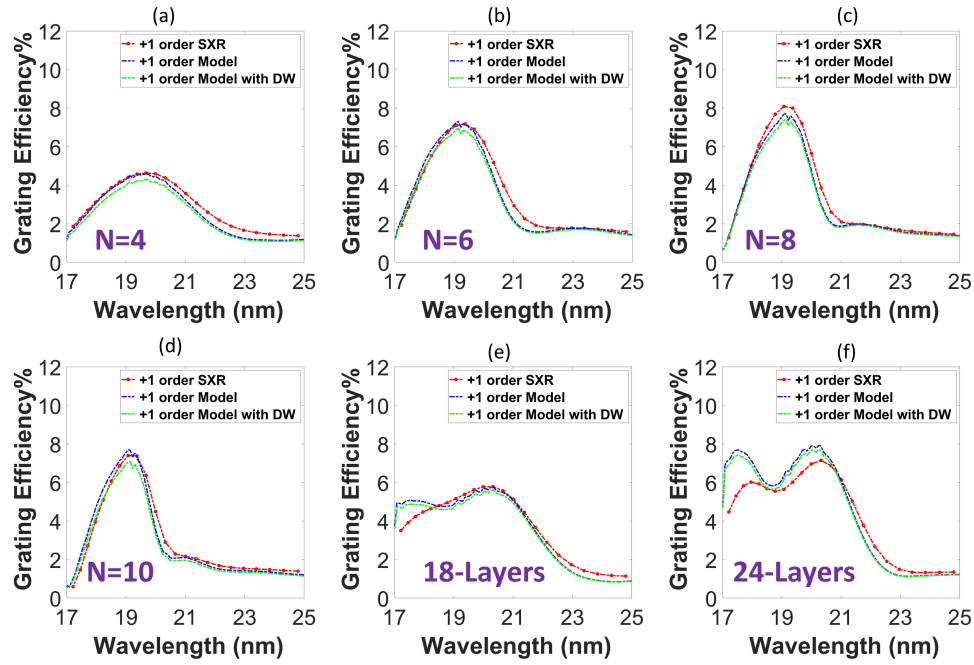The peak efficiency for the periodic multilayers on grating type 1(Fig.13(a-d)) increases from

Fig. 13. Measured and modeled +1 order diffraction efficiency of the multilayer grating type 1 at $\theta = 5°$: (a) $N = 4$, (b) $N = 6$, (c) $N = 8$, (d) $N = 10$, (e) 18 layers aperiodic, and (f) 24 layers aperiodic.

Table 3. Grating type 1 parameter used to simulate +1 order efficiencies in Fig.13.

	h_1 (nm)	α (°)	ff
$N = 4$	7.2	12.0	0.4
$N = 6$	7.0	9.6	0.44
$N = 8$	7.2	9.1	0.44
$N = 10$	7.2	9.3	0.37
Aperiodic Design 1	6.2	9.0	0.38
Aperiodic Design 2	5.8	8.9	0.42

$N = 4$ to $N = 8$ and then decreases at $N = 10$. This is likely due to the change in grating profile shape measured by AFM and confirmed by TEM. As shown in Fig.8, the profile shape remains trapezoidal from $N = 4$ to $N = 8$, but at $N = 10$, it changes to sinusoidal. This change in profile shape can lead to a decrease in diffraction efficiency. On the other hand, the peak efficiency for the periodic multilayers on grating type 2 (Fig.14(a-d)) increases from $N = 4$ to $N = 6$ and then starts to decrease from $N = 8$ to $N = 10$. This agrees with the evolution of the grating profile shown in Fig.9, which remains trapezoidal only in $N = 4$ and becomes sinusoidal from $N = 6$ to $N = 10$.

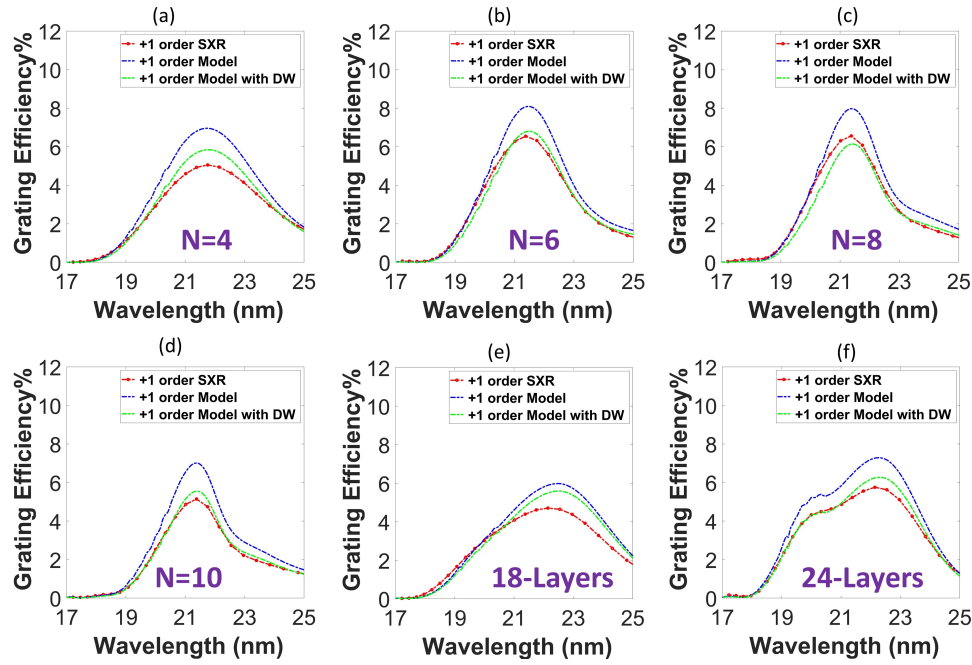The aperiodic designs 1 and 2, with 18 and 24 layers respectively, present a broader bandwidth

Fig. 14. Measured and modeled +1 order diffraction efficiency of the multilayer grating type 2 at $\theta = 5°$: (a) $N = 4$, (b) $N = 6$, (c) $N = 8$, (d) $N = 10$, (e) 18 layers aperiodic, and (f) 24 layers aperiodic.

Table 4. Grating type 2 parameters used to simulate +1 order efficiencies in Fig.14.

	h_2 (nm)	α (°)	ff
$N = 4$	17.6	26.7	0.46
$N = 6$	17.6	25.1	0.43
$N = 8$	17.8	23.7	0.41
$N = 10$	18.0	23.6	0.36
Aperiodic Design 3	17.8	25.0	0.42
Aperiodic Design 4	17.0	23.4	0.42

compared to the periodic designs, despite having a slightly lower peak efficiency (see Fig.13(e) and Fig.13(f)). Similarly, aperiodic designs 3 and 4, which have respectively 18 and 24 layers, show wider bandwidths than the periodic designs. This is likely due to the fact that aperiodic designs can have a more uniform distribution of the multilayer periods, leading to a broader range of wavelengths being diffracted efficiently. These results confirm that the use of aperiodic multilayer on diffraction grating can lead to broader diffraction efficiency bandwidths compared to periodic multilayers.

All the measurements were then modeled using the RCWA method with the grating parameters obtained from Table.3 for grating type 1 and Table.4 for grating type 2. The multilayer material

thicknesses used to model the periodic and aperiodic samples are the theoretical values (see Table.2 and Fig.4). Based on the modeling of the multilayer samples, an oxidation layer is included in the RCWA models. To simplify the RCWA fitting model parameters, the same value of oxide thickness (1.0 nm) was chosen for all samples. In the simulation, the presence of this oxidation layer slightly reduces the amplitude of the +1st diffraction efficiency and causes a slight shift towards shorter wavelengths. Note that the parameters α and ff in Table.3 and Table.4 are average values computed from the AFM grating profiles after deposition in Fig.8 and Fig.9, respectively. The values of h_1 and h_2 were estimated by adjusting the grating depth in the RCWA model until a good agreement was achieved between the measured and simulated +1-order diffraction (see Table.3 and Table.4). The h values derived from RCWA modeling for both grating types 1 and 2 are in good agreement with the AFM measurements after deposition (see Fig.8 and Fig.9). Note that h_1 (or h_2) is the only fitted parameter in the model. The results of the model are plotted in Fig.13 and Fig.14 and show a reasonable agreement with experimental data.

However, due to the fact that the RCWA calculation doesn't take into account any interfacial roughness, the simulated values appear to be higher than the experimental data.

In order to assess the effect of multilayer interfacial roughness on the +1-order diffraction efficiency of the gratings, we decided to use the Debye-Waller factor. The DW factor is a simplified model to account for the effect of roughness and interfacial mixing in multilayer structures [28]. We applied the DW factor to the diffraction efficiency calculated by RCWA (E_{RCWA}), the following equation.1 where σ_{DW} is the DW roughness parameter and E_{DW} the resulting efficiency that accounts for roughness.

$$E_{\text{DW}} = E_{\text{RCWA}} \times \exp\left(-\left[\frac{4\pi \cos(\theta)\sigma_{\text{DW}}}{\lambda}\right]^2\right) \tag{1}$$

For each sample, σ_{DW} is set to the average of the top and bottom roughness values of the grating after the deposition according to the tables in the appendix section. The results plotted in Fig .13 and Fig .14 show that the Debye-Waller model significantly improves the agreement between the simulations and the measurements, indicating the importance of considering roughness and interfacial mixing effects in the design and characterization of multilayer gratings. In particular, due to the higher roughness values for the samples of grating type 2 (see Table.5 and Table.6 in appendix), the Debye-Waller model in Fig .14 shows a significant decrease in the diffraction efficiencies, which are consistent with the +1-order measurements.

The results shown in Fig.13(e) and Fig.14(e) of 18 layers confirm that aperiodic coating provides broadband efficiency, as already demonstrated for 12 layers in reference [6]. In addition, increasing the number of layers to 24 layers achieves the highest efficiency over a broader spectral range (see Fig.13(f) and Fig.14(f)).

Fig.15(a) displays how peak efficiency changes with the number of multilayer periods for grating types 1 and 2. Meanwhile, as shown on Fig.15(b), the bandwidth decreases as the number of multilayer periods increases from $N = 4$ to $N = 10$. The aperiodic designs with 18 layers (design 1) and 24 layers (design 2) on grating type 1 exhibit peak efficiencies of 5.8% and 7.1%, respectively, along with corresponding bandwidths of 3.7 nm and 3.9 nm. For aperiodic designs on grating type 2, the peak efficiencies reach 4.7% and 5.8%, along with bandwidths of 3.5 nm and 3.7 nm, respectively with 18 layers (design 3) and 24 layers (design 4).

Furthermore, the peak efficiencies of grating type 2 samples (both periodic and aperiodic) in Fig.15(a) are lower than the ones of gratings type 1. This may be explained partly by the fact that the initial grating roughness is higher for these samples. Indeed, the effect of roughness can be seen on the simulations in Fig.14(b) and Fig.14(f). In addition, both types of grating are not centered at the same wavelength. In order to get a more straightforward comparison of grating type 1 and type 2, we plotted in Fig.16(a) the simulated efficiency of a 6-period multilayer grating
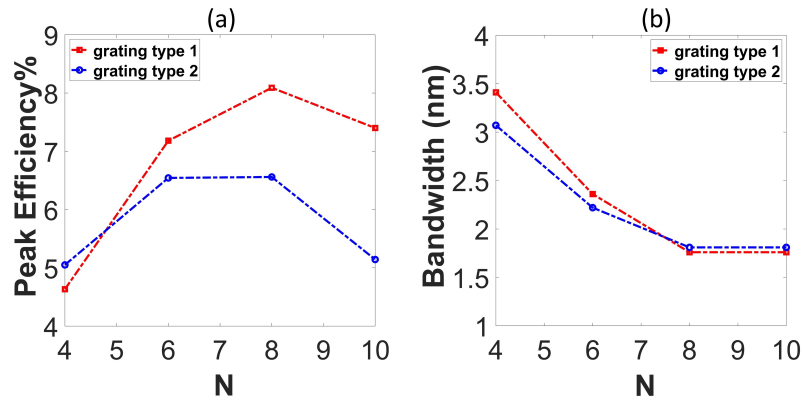
Fig. 15. (a) The peak efficiency for the first diffracted order of grating type 1 and type 2 varied at different values of N. and (b) The bandwidth of the first diffracted order for grating type 1 and type 2 also varied at different values of N.
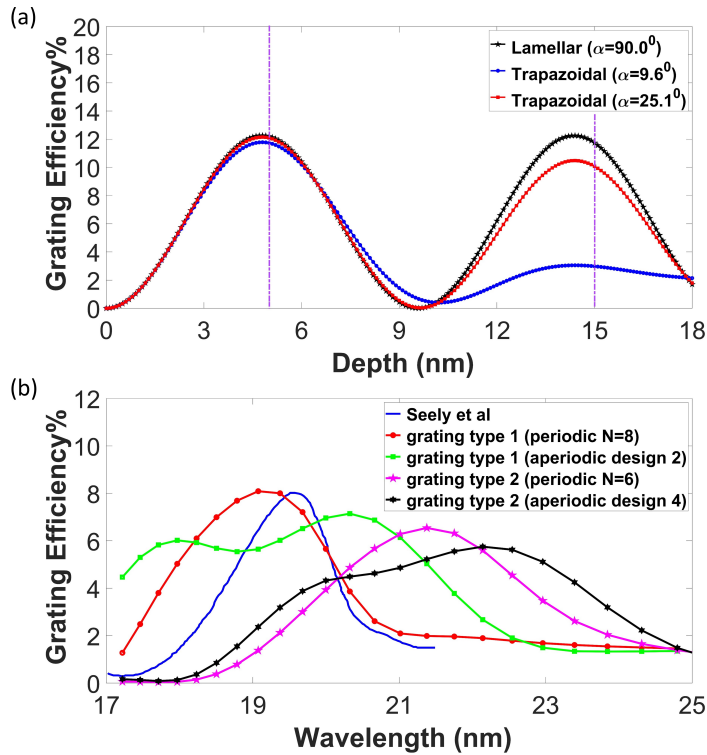

Fig. 16. (a) The efficiency of the 6-periods multilayer grating simulation was affected by changes in the depth of the grating grooves at different values of α while keeping the wavelength constant at 19 nm, and (b) +1 order efficiency measurement at $\theta = 5°$ for the grating type 1 for $N = 8$, 24 layers of aperiodic coatings, and for the grating type 2 for $N = 6$, 24 layers of aperiodic coatings. Experimental data from Seely et al. [29] are also plotted for comparison.

as a function of the groove depth for a wavelength of 19 nm. We used the thickness values of periodic design 1 (see Table 2), a ff of 0.44 (taken from Table 3), and 3 different values for α=

90° (lamellar grating), 25.1° (AFM average value for grating type 2) and 9.6° (AFM average value for grating type 1). For an ideal grating structure ($\alpha = 90°$), Fig.16(a) confirms that both type 1 and type 2 gratings provide the same diffraction efficiency. It's also noticeable that α has minimal impact on the efficiency of the +1-order for a groove depth of 5 nm, which corresponds to the grating type 1. However, when the groove depth is 15 nm (grating type 2), decreasing α leads to a significant decrease in the +1-order diffraction efficiency of the grating. Thus, even if gratings type 1 may be more difficult to fabricate and present lower values of slopes, this study shows that they can attain higher diffraction efficiency in the EUV.

In Fig.16(b), we compare the diffraction efficiency of the best periodic and aperiodic samples for gratings type 1 and 2. It is interesting to note that the peak efficiency for aperiodic designs reaches values similar to the best periodic sample and provides a much wider bandwidth. In the case of grating type 1, the number of deposited layers is the same for periodic ($N = 8$) and aperiodic (24 layers) and the bandwidth is almost twice as wide for the aperiodic design. These results confirm the interest in aperiodic-multilayer coated gratings for spectro-imaging instruments such as Solar C. We have also plotted in Fig. 16(b) for comparison the results previously reported by Seely et al. [29, 30] with a 20-period Mo/Si coated lamellar grating. The peak efficiency and bandwidth achieved by Seely et al. [29] were 8% and 1.1 nm, respectively. In comparison, for grating type 1, the 8-period Al/Mo/SiC multilayer achieved a peak efficiency of 8.1% with a bandwidth of 1.8 nm, while the Al/Mo/SiC aperiodic design 2 attained a high-efficiency plateau with a bandwidth of 3.9 nm.

7. Conclusion

In this study, Al/Mo/SiC periodic and aperiodic multilayers were designed to maximize 1st-order diffraction efficiency in the wavelength ranges of 17-21 nm and 19-23 nm. 4 periodic samples (with N varying from 4 to 10) and 2 aperiodic designs (with 18 and 24 layers) were deposited by magnetron sputtering on two types of grating substrates with a groove density of 4000 l/mm and different groove depths: $\approx$5 nm (grating type 1) and $\approx$16 mn (grating type 2). AFM measurements showed that the top parts of the initial trapezoidal grating profile tend to have a more sinusoidal profile as the number of layers increases for both types of gratings. AFM measurements also reveal that the depth of the grooves increase with the multilayer deposition for these 4000 l/mm grating, which was not the case for the 3600 l/mm grating previously studied [6]. Additional TEM cross-section measurements on 2 multilayer grating samples (one of each type) confirm this grating profile evolution. In addition, the first-order diffraction efficiencies of all multilayer grating samples were measured by SXR and modeled by RCWA. For periodic-multilayer gratings, maximum efficiency is reached for 6 to 8 periods. For a larger number of periods, the efficiency was found to decrease due to the evolution of the grating profile. The RCWA simulations were performed using the multilayer parameters previously determined by analyzing the multilayer designs deposited on flat silicon substrates by GIXR and SXR. The only free parameter in the simulation was the depth of the groove, which was found to vary with the multilayer deposition. The model was further enhanced using the Debye-Waller factor to account for the multilayer interfacial roughness. A good agreement was obtained between simulation and experimental data for all the multilayer grating samples. Furthermore, large bandwidths with peak efficiencies are close to the periodic ones. were achieved by using aperiodic multilayer designs with 24 layers. Finally, experimental results with periodic and aperiodic multilayers also showed that grating type 1 is less sensitive to the slope of the trapezoidal profile and can provide higher efficiency than grating type 2. These results confirm that aperiodic multilayers have great potential for EUV spectroscopy applications. The models derived from this study will allow for designing efficient EUV multilayer gratings for future spectro-imaging instruments.

8. Backmatter

9. Appendix

Table 5. RMS roughness of the surface before and after deposition measured by AFM for grating type 1.

Sample	Before Deposition		After Deposition	
	Top	Bottom	Top	Bottom
$N = 4$	0.25 nm	0.27 nm	0.41 nm	0.41 nm
$N = 6$	0.22 nm	0.36 nm	0.34 nm	0.35 nm
$N = 8$	0.20 nm	0.24 nm	0.31 nm	0.31 nm
$N = 10$	0.24 nm	0.26 nm	0.44 nm	0.44 nm
Aperiodic design 1	0.27 nm	0.36 nm	0.28 nm	0.28 nm
Aperiodic design 2	0.29 nm	0.36 nm	0.27 nm	0.27 nm
Average	0.24 nm	0.31 nm	0.34 nm	0.34 nm

References

1. E. Spiller, "High-performance multilayer coatings for euv lithography," in *Advances in Mirror Technology for X-Ray, EUV Lithography, Laser, and Other Applications,* vol. 5193 (SPIE, 2004), pp. 89–97.
2. C. Tarrio and S. Grantham, "Synchrotron beamline for extreme-ultraviolet multilayer mirror endurance testing," Rev. scientific instruments **76** (2005).
3. Z. Wang, F. Wang, Z. Zhang, H. Wang, W. Wu, S. Zhang, Z. Gu, X. Cheng, B. Wang, S. Qin *et al.*, "Current research activities in the field of multilayer for euv, soft x-ray and x-rays in ipoe," in *ICO20: Optical Design and Fabrication,* vol. 6034 (SPIE, 2006), pp. 97–104.
4. W. Jark, "Enhancement of diffraction grating efficiencies in the soft x-ray region by a multilayer coating," Opt. communications **60**, 201–205 (1986).
5. Y. Feng, Q. Huang, Y. Zhuang, A. Sokolov, S. Lemke, R. Qi, Z. Zhang, and Z. Wang, "Mo/si lamellar multilayer gratings with high efficiency and enhanced resolution for the x-ray region of 1000–1700 ev," Opt. Express **29**, 13416–13427 (2021).
6. A. H. K. Mahmoud, S. de Rossi, E. Meltchakov, B. Capitanio, M. Thomasset, M. Vallet, E. Héripré, and F. Delmotte, "Al/mo/sic multilayer diffraction gratings with broadband efficiency in the extreme ultraviolet," Opt. Express **30**, 38319–38338 (2022).
7. D. Voronov, E. Anderson, R. Cambie, S. Cabrini, S. Dhuey, L. Goray, E. Gullikson, F. Salmassi, T. Warwick, V. Yashchuk *et al.*, "A 10,000 groove/mm multilayer coated grating for euv spectroscopy," Opt. Express **19**, 6320–6325 (2011).

Table 6. RMS roughness of the surface before and after deposition measured by AFM for grating type 2.

Sample	Before Deposition		After Deposition	
	Top	Bottom	Top	Bottom
$N = 4$	0.30 nm	0.30 nm	0.89 nm	0.56 nm
$N = 6$	0.44 nm	0.48 nm	0.91 nm	0.52 nm
$N = 8$	0.65 nm	0.83 nm	1.15 nm	0.60 nm
$N = 10$	0.47 nm	0.47 nm	1.20 nm	0.45 nm
Aperiodic design 1	0.32 nm	0.37 nm	0.53 nm	0.40 nm
Aperiodic design 2	0.38 nm	0.48 nm	0.69 nm	0.69 nm
Average	0.43 nm	0.49 nm	0.90 nm	0.54 nm

8. D. Voronov, E. Gullikson, F. Salmassi, T. Warwick, and H. Padmore, "Enhancement of diffraction efficiency via higher-order operation of a multilayer blazed grating," Opt. letters **39**, 3157–3160 (2014).

9. S. Bajt, H. N. Chapman, A. Aquila, and E. Gullikson, "High-efficiency x-ray gratings with asymmetric-cut multilayers," JOSA A **29**, 216–230 (2012).

10. P. Pradhan, S. Bhartiya, A. Singh, A. Majhi, A. Gome, R. Dhawan, M. Nayak, P. Sahoo, S. Rai, and V. Reddy, "Fabrication and characterization of w/b4c lamellar multilayer grating and nbc/si multilayer phase-shift reflector," in *Advances in X-Ray/EUV Optics and Components XII*, vol. 10386 (SPIE, 2017), pp. 17–25.

11. X. Yang, I. V. Kozhevnikov, Q. Huang, H. Wang, M. Hand, K. Sawhney, and Z. Wang, "Analytic theory of alternate multilayer gratings operating in single-order regime," Opt. Express **25**, 15987–16001 (2017).

12. Y. Feng, L. Du, Q. Huang, Z. Liu, A. Sokolov, R. Qi, X. Yang, Z. Zhang, and Z. Wang, "Cr/c lamellar multilayer grating in conical diffraction mounting for beam splitter used in x-ray free-electron lasers," Opt. Lett. **47**, 1331–1334 (2022).

13. F. Choueikani, B. Lagarde, F. Delmotte, M. Krumrey, F. Bridou, M. Thomasset, E. Meltchakov, and F. Polack, "High-efficiency b 4 c/mo 2 c alternate multilayer grating for monochromators in the photon energy range from 0.7 to 3.4 kev," Opt. Lett. **39**, 2141–2144 (2014).

14. E. Meltchakov, C. Hecquet, M. Roulliay, S. De Rossi, Y. Menesguen, A. Jérome, F. Bridou, F. Varniere, M.-F. Ravet-Krill, and F. Delmotte, "Development of al-based multilayer optics for euv," Appl. Phys. A **98**, 111–117 (2010).

15. P. Rochus, F. Auchere, D. Berghmans, L. Harra, W. Schmutz, U. Schühle, P. Addison, T. Appourchaux, R. A. Cuadrado, D. Baker *et al.*, "The solar orbiter eui instrument: the extreme ultraviolet imager," Astron. & Astrophys. **642**, A8 (2020).

16. T. Shimizu, S. Imada, T. Kawate, Y. Suematsu, H. Hara, T. Tsuzuki, Y. Katsukawa, M. Kubo, R. Ishikawa, T. Watanabe *et al.*, "The solar-c (euvst) mission: the latest status," in *Space Telescopes and Instrumentation 2020: Ultraviolet to Gamma Ray*, vol. 11444 (SPIE, 2020), pp. 113–119.

17. D. L. Windt, "Imd—software for modeling the optical properties of multilayer films," Comput. physics **12**, 360–370 (1998).

18. "Cxro x-ray interactions with matter," http://henke.lbl.gov/optical_constants/. Accessed: 2021-07-01.

19. J. P. Hugonin and P. Lalanne, "Reticolo software for grating analysis," arXiv preprint arXiv:2101.00901 (2021).

20. J. Gautier, F. Delmotte, M. Roulliay, F. Bridou, M.-F. Ravet, and A. Jérome, "Study of normal incidence of three-component multilayer mirrors in the range 20–40 nm," Appl. optics **44**, 384–390 (2005).

21. I. Horcas, R. Fernández, J. Gomez-Rodriguez, J. Colchero, J. Gómez-Herrero, and A. Baro, "Wsxm: A software for scanning probe microscopy and a tool for nanotechnology," Rev. scientific instruments **78** (2007).

22. I. Kock, T. Edler, and S. G. Mayr, "Growth behavior and intrinsic properties of vapor-deposited iron palladium thin films," J. Appl. Phys. **103** (2008).

23. E. Meltchakov, S. De Rossi, R. Mercier, F. Varniere, A. Jérome, F. Auchère, X. Zhang, M. Roulliay, and F. Delmotte, "Single and multi-channel al-based multilayer systems for space applications in euv range," in *Damage to VUV, EUV, and X-ray Optics IV; and EUV and X-ray Optics: Synergy between Laboratory and Space III*, vol. 8777 (SPIE, 2013), pp. 288–296.

24. X. Yang and T.-C. Weng, "A compact extreme ultraviolet high-throughput spectrometer based on the multilayer

varied-line-spacing grating," Rev. Sci. Instruments **92** (2021).

25. X. Yang, I. V. Kozhevnikov, Q. Huang, H. Wang, K. Sawhney, and Z. Wang, "Wideband multilayer gratings for the 17–25 nm spectral region," Opt. Express **24**, 15079–15092 (2016).

26. J. Rebellato, E. Meltchakov, R. Soufli, S. De Rossi, X. Zhang, F. Auchère, and F. Delmotte, "Analyses of tabulated optical constants for thin films in the euv range and application to solar physics multilayer coatings," in *Advances in Optical Thin Films VI,* vol. 10691 (SPIE, 2018), pp. 200–215.

27. J. Schindelin, I. Arganda-Carreras, E. Frise, V. Kaynig, M. Longair, T. Pietzsch, S. Preibisch, C. Rueden, S. Saalfeld, B. Schmid *et al.*, "Fiji: an open-source platform for biological-image analysis," Nat. methods **9**, 676–682 (2012).

28. E. Spiller, *Soft X-ray optics*, vol. 15 (SPIE press, 1994).

29. J. F. Seely, C. M. Brown, D. L. Windt, S. Donguy, and B. Kjornrattanawanich, "Normal-incidence efficiencies of multilayer-coated laminar gratings for the extreme-ultraviolet imaging spectrometer on the solar-b mission," Appl. optics **43**, 1463–1471 (2004).

30. J. F. Seely, "Multilayer grating for the extreme ultraviolet spectrometer (eis)," in *X-Ray Optics, Instruments, and Missions IV,* vol. 4138 (SPIE, 2000), pp. 174–181.